

Design and Synthesis of Sm, Y, La and Nd doped CeO₂ with a broom like hierarchical structure: a photocatalyst with enhanced oxidation performance

著者	Xu Bin, Yang Hui, Zhang Qitao, Yuan Saisai, Xie An, Zhang Ming, Ohno Teruhisa
journal or publication title	ChemCatChem
volume	12
number	9
page range	2638-2646
year	2020-03-09
URL	http://hdl.handle.net/10228/00008049

doi: <https://doi.org/10.1002/cctc.201902309>

FULL PAPER

Design and Synthesis of Sm, Y, La and Nd-doped CeO₂ with a broom-like hierarchical structure: a photocatalyst with enhanced oxidation performance

Bin Xu,^{*[a]} Hui Yang,^[a] Qitao Zhang,^{*[b]} Saisai Yuan,^[c] An Xie,^[a] Ming Zhang,^[a] Teruhisa Ohno^{*[d]}

[a] B. Xu, H. Yang, A. Xie, M. Zhang,
School of Chemistry and Chemical Engineering
Yangzhou University
Yangzhou, 225009, China
E-mail: twt@yzu.edu.cn

[b] Q. Zhang
International Collaborative Laboratory of 2D Materials for Optoelectronics Science and Technology of Ministry of Education, Institute of Microscale Optoelectronics
Shenzhen University
Shenzhen, 518060, China
E-mail: qitao-zhang@szu.edu.cn

[c] S. Yuan
Department of Chemical and Biochemical for Energy Materials
Xiamen University
Xiamen, 361005, China
E-mail: yuansaisai66666@163.com

[d] T. Ohno
Department of Applied Chemistry, Faculty of Engineering
Kyushu Institute of Technology
Kitakyushu, 804-8550, Japan
E-mail: tohno@che.kyutech.ac.jp.

Abstract: CeO₂ doped with various rare earth (RE) ions (Sm, Y, La and Nd) having a broom-like hierarchical structure was successfully prepared by a template-free hydrothermal method. The photooxidation performance of RE-doped products was significantly better than that of pure CeO₂, and comparative experiments showed that Sm-doped CeO₂ (SC) has superior photooxidation activity, resulting about 3.0-times and 8.5-times higher activities of bisphenol A (BPA) degradation and of acetaldehyde (CH₃CHO) decomposition, respectively, than those of pure CeO₂. Due to the incorporation of RE ions, the surface exposed cerium ions are partly substituted by those cations, resulting in a higher concentration of oxygen vacancies (O_v) in RE-doped CeO₂. The increased O_v can act as a trapping center for photo-generated electrons to form a doping transition state between the conduction band (CB) and valence band (VB), which can restrict the recombination rate of electrons and holes effectively and lead to an outstanding enhancement of photooxidation performance. Furthermore, abundant highly reactive hydroxyl radicals ($\cdot\text{OH}$) and superoxide radicals ($\cdot\text{O}_2^-$), which are efficient intermediates with vivid oxidation ability, can further enhance the photocatalytic activity of RE-doped CeO₂. A cost-effective strategy for designing CeO₂-based semiconductor photocatalysts doped with multitudinous RE ions that have enhanced photooxidation performance is presented in this paper.

Introduction

Recently, human health and ecosystems have been threatened by a serious threat to environmental pollution mainly due to organic pollutants and toxic gas wastes generated in industrialization process.^[1-3] Novel photocatalytic materials for elimination of multi-species pollutants from industrial streams have been developed.^[2-4] However, newly developed materials have some problems such as a high rate of recombination of photogenerated electrons and holes, poor photo-chemical stability and weak visible light absorption, which greatly hinder

their popularization and application as cost-efficient semiconductor photocatalysts.^[2, 3]

Cerium dioxide (CeO₂) is one of the most important rare earth metal oxides, and it has attracted much attention due to its excellent properties such as low toxicity, high degree of chemical stability, safety and resistance to photocorrosion primarily.^[4] It has various applications including applications as UV blockers, polishing materials, photocatalysts, electrolytes, sensors and fuel cells.^[5] In addition, the photocatalytic properties of CeO₂ are similar with those of TiO₂-based materials including a wide band gap (2.90 eV) and strong absorption in the UV region. It is therefore a promising candidate material for photocatalytic degradation of deleterious organic pollutants. Previous studies have shown that morphology and size control, doping of various metal ions, and heterojunction coupling are three common strategies for enhancing the photocatalytic performance of CeO₂-based materials.^[5, 6] The morphology of CeO₂ plays a major role in its photocatalytic performance, and our research group has successfully fabricated a series of high-performance CeO₂ photocatalysts with different morphologies and superior performances including porous broom-like, hedgehog-like, confeito-like and hollow octahedral structures.^[7-9] Difference in morphology and size can determine the specific surface area, active sites and separation of redox crystal facets, which are related to improvement of photocatalytic performance. Choudhury has studied the effect of [Ce³⁺] and oxygen vacancies on the photocatalytic activity of CeO₂.^[10] The large deviated stoichiometry of CeO₂ makes it easier for cerium ions to be reduced from tetravalent cerium to trivalent cerium and enhance the formation of active oxygen vacancies (O_v).^[11-13] The effectiveness of pure CeO₂ also can be improved by introducing foreign metal ions to promote the formation of expanded crystal-structured CeO₂-based products, which are more convenient for electronic transmission.^[14] Some studies have indicated that the introduction of various metal dopant such as Fe, Eu and Mn can

change the structure and optical properties of CeO₂.^[15-17] Studies have also shown that the presence of metal ions in the ceria lattice induced more trivalent ceria ions and oxygen vacancies, which are more important for photocatalytic pollution degradation.^[11] The key point of these methods is the change in the oxygen vacancies concentration of the products, which can serve as electron-capture centers.^[10] Thus, the as-formed oxygen vacancies can also effectively suppress the recombination of electron-hole pairs, thereby improving the final photocatalytic activity.^[16-22] Therefore, doping of foreign ions a cost-effective way to enhance the activity of a CeO₂-based photocatalyst. To the best of our knowledge, it is very difficult to introduce different ions into the lattice of ceria, and there has been no report about a summary of CeO₂ with doping a series of different RE ions and elucidation of the effects on photocatalytic performance systematically.

In this paper, CeO₂ materials doped with several rare earth ions (Sm, Y, La and Nd) that have a broom-like hierarchical structure were prepared by a template-less hydrothermal method. The photooxidation efficiency of the samples were evaluated by experiments on aqueous BPA degradation and on CO₂ evolution from CH₃CHO decomposition. Furthermore, the morphology, structure and photoelectrochemical properties were examined to determine the effect of RE ions doping. Due to an increasing concentration of oxygen vacancies, photooxidation performance of RE-doped products was significantly better than that of pure CeO₂, and the results of comparative experiments showed that Sm-doped CeO₂ has the best photooxidation activity. Thus, doping with appropriate ions is effective for enhancing the photocatalytic activity of a bulk photocatalyst.

Results and Discussion

The morphology of as-prepared products was investigated by FE-SEM and HR-TEM. As exhibited in Figure 1a, pure CeO₂ shows a broom-like hierarchical morphology with a single root length of 5 μm and diameter of 200 nm approximately. Clear lattice fringes with interplanar spacing of 0.313 nm, which are assigned to the CeO₂ (111) crystal plane, can be seen in Figure 1A. After doping with different RE ions, the products still maintain the broom-like hierarchical structure (Figure 1b-e). However, there are distinct changes in the degree of surface smoothness and average diameter and length of the nanorods. It is notable that the lattice fringes in the RE-doped products have interplanar spacing: SC (0.320 nm), YC (0.314 nm), LC (0.328 nm) and NC (0.325 nm) (Figure 1B-E). The alteration in lattice spacing indicates that those RE ions have been successfully introduced into the interior lattice of CeO₂, but the crystal structure of ceria's cubic fluorite is in fact preserved.

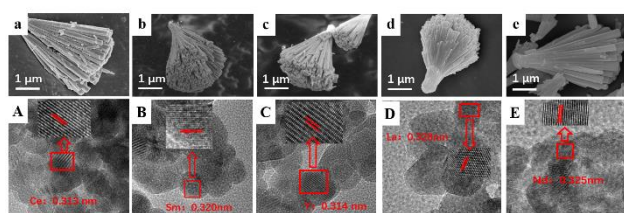


Figure 1. FE-SEM and HR-TEM images: (a, A) CeO₂, (b, B) SC, (c, C) YC, (d, D) LC and (e, E) NC.

EDS mapping results (Figure 2) indicate that only cerium and oxygen elements are clearly detected in pure CeO₂ and are evenly distributed among the nanorods. After the introduction of RE ions, doping elements except for Ce and O also have a good distribution on the surface (Figure 2b-e). In view of the above results, it can be further inferred that photocatalysts doped with different RE ions can be successfully prepared by a hydrothermal treatment.

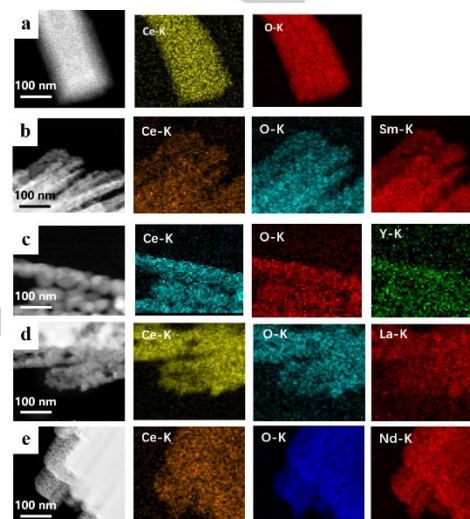


Figure 2. HAADF image and distribution of element mapping images: (a) CeO₂, (b) SC, (c) YC, (d) LC and (e) NC.

XRD patterns of as-fabricated samples are shown in Figure 3a. The characteristic diffraction peaks of CeO₂ are located at 28.60°, 33.27°, 47.71° and 56.51°, corresponding to the crystal planes of (111), (200), (220) and (311), respectively.^[22, 23] All of the diffraction lines can be attributed to the phase of ceria with a cubic fluorite structure (space group: Fm-3m (225)), which is in accordance with the standard data reported in the JCPDS card (No. 65-5923).^[23-24] The sharp diffraction peaks of products suggest a high degree of crystallinity, and no appearance of impurity peaks manifests that doping has a negligible effect on crystal growth. Compared with pure CeO₂, the elaborated XRD patterns (Figure 3b) of the highest (111) peak exhibit an obvious shift to a lower angle after doping. This phenomenon can be conspicuously attributed to the introduction of rare earth ions into the crystal structure.^[24] And these results are consistent with the changes in lattice fringes observed in HR-TEM.

Rietveld refinement was further carried out to determine the actual doping location of incorporated ions and the results are summarized in Table S1. It can be clearly seen that the lattice parameter values of RE-doped samples become larger than that of pure CeO₂ (5.4114 Å). The values are 5.4182 Å, 5.4290 Å, 5.4219 Å and 5.4211 Å for SC, YC, LC, and NC, respectively. In comparison to Ce⁴⁺ (0.970 Å), the enlarged lattice parameters can be attributed to the larger ionic radius of various rare earth element ions such as Sm³⁺ (1.079 Å), Y³⁺ (1.019 Å), La³⁺ (1.160 Å), Nd³⁺ (1.109 Å). In the MO₆ crystal structure of ceria, the substitution reaction is more likely to occur on cerium atoms located on the top and edge than in the body center. When the rare earth ions have been introduced into the crystal structure of CeO₂, its crystal lattice would be greatly expanded. It is well

known that an expanded crystal structure is more beneficial than normal MO_8 crystal structure for electronic transmission.^[25]

Raman technology is an effective and non-destructive technique for characterizing structural defects.^[26] The distinct peak at 460 cm^{-1} is assigned to F_{2g} vibration of the cubic fluorite structure as illustrated in Figure 3c. Two weak Raman peaks located at 540 cm^{-1} and 600 cm^{-1} were also detected, and they are ascribed to extrinsic defects caused by doping (R_{dopant}) and instinctive defect vibration of Ce-O ($R_{\text{Ce-O}}$), respectively.^[27-29] An enlarged view of Raman peaks is shown in Figure 3d. According to the results of previous studies,^[30] cerium ions show a trivalent state instead of tetravalent chemical valence in the defect lattice partly. In order to maintain the particles in an electrically neutral state, surface oxygen would escape from the structure, eventually resulting in the formation of inherent oxygen vacancies (O_v).^[31] Later, more oxygen vacancies would promote the separation of charge carriers and limit the recombination rate of photo-generated carriers. The relative photocatalytic performance would be enhanced. The relativity intensity of a Raman shift of F_{2g} , R_{dopant} and $R_{\text{Ce-O}}$ can be calculated from Equation (1).^[30, 31]

$$\frac{\text{O}_v}{F_{2g}} \% = \frac{A_{\text{era}R_{\text{Ce-O}}} + A_{\text{era}R_{\text{dopant}}}}{A_{\text{era}F_{2g}}} \% \quad (1)$$

The calculated values are outlined in Table S2. Compared with pure CeO_2 , the values of O_v clearly increase after RE ion doping. And the value of O_v reaches a maximum of 12.50% after Sm doping, being consistent with the result of XPS analysis shown below.

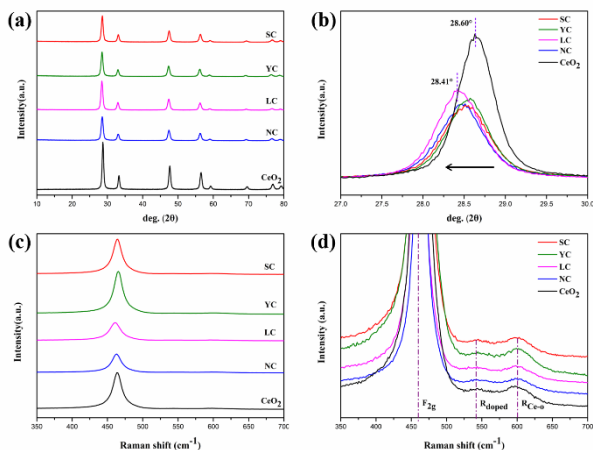


Figure 3. Structure characterization: (a) XRD patterns, (b) detailed view of the highest (111) peak patterns, (c) Raman spectra and (d) enlarged view of Raman spectra.

The surface chemical composition and the interactions before and after doping were analyzed by XPS spectroscopy (Figure S1 & Figure S2). The Ce3d electron core level and two group peaks obtained (denoted as v and u) after deconvolution treatment are displayed in Figure 4a. According to previous studies,^[31, 32] the labels of (U, V), (U_2 , V_2) and (U_3 , V_3) can be classified as Ce $3d_{5/2}$ and Ce $3d_{3/2}$ related to Ce^{4+} , originating from the final states of Ce ($3d^9 4f^0$) O ($2p^6$), Ce ($3d^9 4f^1$) O ($2p^5$) and Ce ($3d^9 4f^2$) O ($2p^4$), respectively. Two pairs of doublets, (U_0 , V_0) and (U_1 , V_1), for the Ce 3d bond energy peak can be ascribed to Ce^{3+} , and the double lines correspond to Ce ($3d^9 4f^1$) O ($2p^6$) and Ce

($3d^9 4f^1$) O ($2p^5$), respectively.^[31, 32] In order to estimate the concentration of $[\text{Ce}^{3+}]$ of samples, these peaks were deconvoluted and the calculated concentration value of as-prepared samples are shown in Table S2. The $[\text{Ce}^{3+}]$ ratio is obviously increased after RE ions doping, which is much higher than the product without doping. Meanwhile, the concentration of $[\text{Ce}^{3+}]$ of SC is 17.69%, which is the highest among the products of doping. In addition, these peaks significantly shift to a lower binding energy and it manifests that Sm ions indeed dope into the lattice of CeO_2 (Figure 4b). Therefore, it can be understood that the introduction of dopants greatly influences the chemical environment of Ce-O by the reduction of $\text{Ce}^{4+} \rightarrow \text{Ce}^{3+}$, which is a foremost reason for the increased concentration in oxygen vacancies, which are beneficial for enhancing photocatalytic efficiency when compared with pure CeO_2 .^[10]

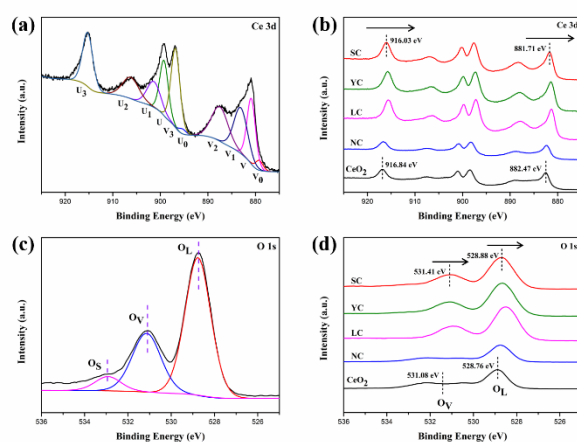
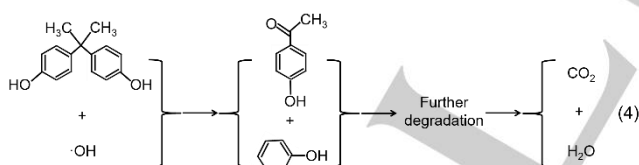
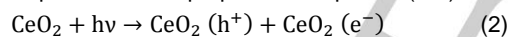


Figure 4. Separated peak curves of (a) Ce 3d, (c) O 1s, high-resolution XPS spectra of (b) Ce 3d, and (d) O 1s of all samples.

Three different types of oxygen species, assigned to lattice oxygen (O_{lat}), oxygen vacancies (O_v) and active surface oxygen (O_{Sur}), can be clearly detected after deconvolution of the O1s electron core level located binding energy of 528.76, 531.08, and 532.95 eV, respectively (Figure 4c).^[33] The binding energy of these oxygen species significantly shifts towards lower binding energy after doping of RE ions. However, the effects on O_{lat} , O_v and O_{Sur} are quite different. Compared with pure CeO_2 , the binding energy value of O_v shows a change of 0.33 eV after Sm doping. The binding energy value of the O_{lat} and O_{Sur} shows changes of only 0.12 eV and 0.20 eV, respectively. (Figure 4d). Therefore, RE ions doping mainly affects the binding energy of O_v . The O_v ratio after deconvolution and multimodal separation is obtained in Table S2. It can be observed that the concentration of $[\text{O}_v]$ in doped- CeO_2 is much higher than that in pure CeO_2 , while a similar phenomenon exists for $[\text{Ce}^{3+}]$. In particular, the concentrations of $[\text{Ce}^{3+}]$ and $[\text{O}_v]$ in SC are 17.69% and 15.25%, respectively, which are significantly higher than other products. It may due to the substitution process can compensate for the charge generated by doping and promote the formation of oxygen vacancies in defective structured CeO_2 . And these vivacious O_v , acting as a trapping center for photo-generated electrons, formed a doping transition state between the conduction band (CB) and valence band (VB), and limited the recombination rate of electrons and holes significantly, leading to an outstanding improvement of photooxidation performance effectively.^[7] Therefore, it provides a

forceful evidence to speculate that RE-doped CeO₂ should have higher photocatalytic activity.^[33, 34]

Firstly, photooxidation activity of as-prepared products was evaluated by degradation of aqueous bisphenol A (BPA). The BPA removal rate of SC reaches 98.76% under light irradiation for 6 h (Figure 5a), which is significantly better than that of other samples. The lowest rate constant for photocatalytic degradation activity obtained for the pure CeO₂ is only 34.07%. According to the kinetic equation (Figure 5b), the rate constant k value of SC is 0.5145 h⁻¹, and SC possesses 1.32-, 3.31-, 4.31-, and 5.30-times higher than those of YC, LC, NC and pure CeO₂, respectively. Besides, the tendency of $-\ln(C_t/C_0)$ as a function of irradiation time is displayed in Table S3. It can be concluded that the linear relationship between $-\ln(C_t/C_0)$ and irradiation time follows the pseudo-first order kinetic equation, where C_0 is the initial concentration of BPA and C_t is the concentration at a particular time. After numerical calculation, the rate constant indicates that BPA degradation obeys the Langmuir-Hinshelwood rate. For investigating the BPA photocatalytic degradation process, HPLC was used to analyze the products of each stage. The peak of retention time of 7.74 min is mainly attributed to BPA, and the intensity of the peak decreases gradually during the reaction process, indicating that BPA is degraded continuously (Figure S3). A new peak located at a retention time of 4.04 min appears after photodegradation for two hours, corresponding to p-hydroxyacetophenone, and the intensity gradually increases. Therefore, it should be a major degradation product. In addition, a weak peak at 5.09 min belongs to phenol, and its intensity increases with increase in reaction time. The results of HPLC show that p-hydroxyacetophenone and phenol are the main intermediate products during BPA degradation. These intermediate products may be further oxidized and decomposed, and the final products are non-toxic CO₂ and H₂O. Hence, the following reaction processes are proposed in Equation (2-4):



The BPA degradation pathways have already been established, and it is also necessary to identify the main active substance in the degradation process by trapping experiments.^[35, 36] As demonstrated in Figure 5c, the photodegradation efficiency of BPA decreases rapidly from 98.76% to 12.83% after adding TBA, indicating that $\cdot\text{OH}$ is one of the main active species in the BPA photodegradation process. When EDTA was added, the degradation efficiency was also reduced to 17.87%, indicating that h^+ also plays an important role in the photocatalytic oxidation reaction. However, the degradation efficiency of BPA is slightly reduced after the addition of KPS (88.92%) and BQ (84.47%). Generally, obvious reduction of photocatalytic efficiency indicates that the corresponding substance owns an important effect.³⁴⁻³⁶ Consequently, the results of the active substance capture experiments indicate that $\cdot\text{OH}$ and h^+ are the main active substances, while $\cdot\text{O}_2^-$ and e^- have minor effects on the

degradation of BPA in this RE-doped CeO₂ system. Besides, SC has no significant attenuation after four cycles of BPA photooxidation degradation (Figure 5d), indicating the as-fabricated SC photocatalyst retains excellent photocatalytic stability. Meanwhile, YC, LC, NC and pure CeO₂ also maintain a good reusability.

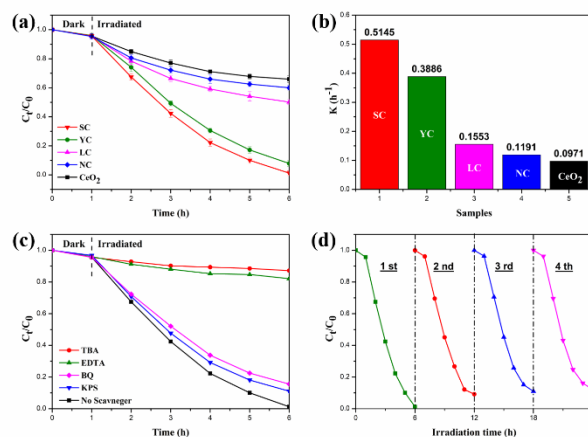
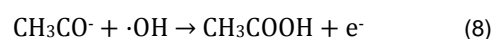
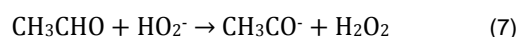
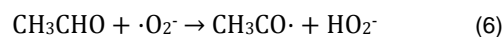


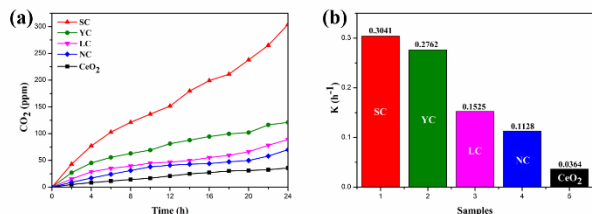
Figure 5. (a) BPA photooxidation degradation curves, (b) degradation kinetics constants, (c) degradation efficiency with the addition of scavengers and (d) stability test.

The photooxidation activity of products was further evaluated from the photocatalytic decomposition of gaseous acetaldehyde (CH₃CHO). And the following reactions can be considered in Equation (5-9):



Compared with pure CeO₂, the photocatalytic activity is clearly enhanced after RE ions doping (Figure 6a). In the case of Sm doping, the amount of CO₂ liberation reaches a maximum of about 304.05 ppm, which is 8.50-times higher than that of pure CeO₂ (35.76 ppm). The excellent photocatalytic activity is attributed to the concentration of O_v, reaching a maximum value in SC, and the results are consistent with results of Raman and XPS analyses. The process of CH₃CHO decomposition follows the first-order kinetic equation obviously (Figure 6b). According to the kinetic equation, the rate constant value of SC reaches 0.3041 h⁻¹ and is clearly higher than other values (YC (0.2762 h⁻¹), LC (0.1525 h⁻¹), NC (0.1128 h⁻¹), CeO₂ (0.0364 h⁻¹)). The SC photocatalyst as-fabricated in this paper shows much higher activity for CH₃CHO (340 ppm) oxidation than the activities of commercial metal oxide photocatalysts such as TiO₂ (21 ppm), S-doped TiO₂ (150 ppm) and WO₃ (200 ppm).^[37, 38] It also shows much higher activity than the other CeO₂ photocatalysts with different morphologies including nanoparticles (200 ppm),

1 hedgehog-like (140 ppm), confeito-like (100 ppm) and octahedral
2 structures (80 ppm).^[7-9]



3
4
5
6
7
8
9
10
11
12 **Figure 6.** (a) Time course of CO₂ liberation from acetaldehyde decomposition and (b) kinetics curves of all samples.

13
14
15
16 The optical effect of dopant ion substitution into the CeO₂
17 lattice was further confirmed using UV-vis absorption spectra
18 (Figure 7a). For semiconductors, the absorption edge of the band
19 follows Equation (10):

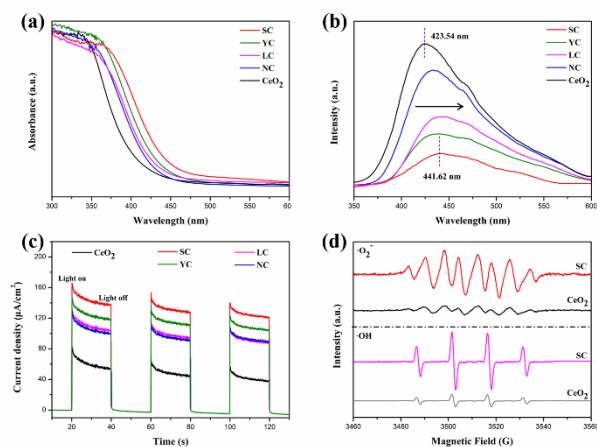
$$20 \quad (\alpha h\nu)^n = B(h\nu - E_g), \quad (10)$$

21
22 where α is the absorption coefficient, B is the material-related
23 constant, $h\nu$ is the discrete photon energy, E_g is the absorption
24 bandgap, and n is the number of different types of electronic
25 transitions.^[39] It has been shown the electronic transition between
26 the valence band and conduction band of CeO₂ is a direct
27 transition, resulting in the value of n being 2.^[40, 41] The Schuster-
28 Kubelka-Munk equation is considered to be reliable for
29 determining a semiconductor bandgap. The band gap values of
30 CeO₂, SC, YC, LC and NC were calculated to be 2.87, 2.59, 2.65,
31 2.74 and 2.79 eV, respectively (Figure S4). The results indicate
32 that rare earth ions doping can induce narrowing of the band gap
33 of CeO₂. A smaller band gap energy (E_g) is considered to be one
34 of the crucial parameters for determining the final photocatalytic
35 performance.^[42] The doping of cations can favor the formation of
36 trivalent cerium (Ce³⁺) and create more oxygen vacancies (O_v).
37 An increasing concentration of O_v can also result in the formation
38 of a doping-related transition state which is closer to the
39 conduction band (CB) and reduce the band gap energy.⁴³ The
40 potential of the valence band (VB) was determined from a VB-
41 XPS spectrum (Figure S5). The results clearly revealed that the
42 rare earth dopant was indeed incorporated into the crystal lattice
43 of CeO₂, resulting in alteration in the electronic properties of the
44 RE ions doping products.^[39-41, 43]

45
46 Photoluminescence (PL) analysis has also been frequently
47 used to determine the recombination rate of electrons and holes
48 (e⁻ and h⁺).⁴⁴ Pure CeO₂ shows a strong characteristic PL peak
49 with a value of about 423.54 nm and a weaker peak of about
50 441.62 nm (Figure 7b). The two peaks are both attributed to
51 surface defects, which are usually accommodated between the
52 O_{2p} valence band and the Ce4f conduction band. It is well known
53 that the major surface defects in CeO₂ are oxygen vacancies.^[45]
54 The doped CeO₂ samples showed emission spectra with the
55 same number of peaks. However, the intensity of the emission
56 band was reduced for CeO₂ doped with different RE ions. SC
57 showed the lowest PL intensity among all the RE-doped CeO₂
58 samples. This indicates an excellent efficiency of promoting
59 separation of holes and electron pairs, which can efficaciously
60 enhance the photocatalytic performance.^[45]

A photocurrent-time response test was carried out to
examine the interface charge separation kinetics, and the results
are shown in Figure 7c. The photocurrent response curves show
that the photocurrent intensity of all samples suddenly increases
and decreases when the light source is turned on and off
respectively, indicating their intrinsic properties of the
semiconductor.^[37, 46] The photocurrent intensities of RE ion-doped
samples (SC (142.83 $\mu\text{A}/\text{cm}^2$), YC (124.58 $\mu\text{A}/\text{cm}^2$), LC (104.68
 $\mu\text{A}/\text{cm}^2$), NC (109.08 $\mu\text{A}/\text{cm}^2$)) are all higher than that of pure
CeO₂ (61.21 $\mu\text{A}/\text{cm}^2$). Interestingly, the photocurrent intensity of
SC reaches a maximum value that is 2.33- times greater than that
of pure CeO₂. The increasing photocurrent intensity indicates that
the photogenerated charge carriers in SC are much more
effectively separated than those in other samples. In general, a
greater intensity of the photocurrent means higher transfer
efficiency of photogenerated electrons and holes, which is
beneficial for the photocatalytic reactions and affords better
photocatalytic performance.^[16]

The EPR results (Figure 7d) further revealed the main active
species. It can be clearly observed that the intensity of hydroxyl
radicals ($\cdot\text{OH}$) and superoxide radicals ($\cdot\text{O}_2^-$) is stronger than that
of pure CeO₂ after Sm doping, being in good agreement with the
results of the active species trapping experiments. Actually, the
formation of $\cdot\text{OH}$ and $\cdot\text{O}_2^-$ is important for photocatalytic reactions
due to both of them are highly efficient intermediates to further
promote the photocatalytic activity. Hence, SC can achieve a
significant improvement in photooxidation performance.



61
62
63
64
65 **Figure 7.** Photoelectrochemical characterization: (a) UV-vis diffuse reflectance spectra, (b) PL spectra, (c) transient photocurrent response curves, and (d) EPR spectra.

Stoichiometric CeO₂ is known to be an insulator, and the
features of the electronic density of states (DOS) calculated in
Figure 8 are in agreement with previous DFT + U results. And it
can be further used to revealing the modifications in electronic
structure and the mechanism of light absorption. Compared with
pure CeO₂, it is evident that conduction bands of RE-doped
structures are shifted from a higher energy level to a lower energy
level. Meanwhile, the doping energy level of SC and NC appeared
obviously. This indicates a narrowed band gap may cause a
reduction of photo-electron transition energy. At the same time,
doping will regulate the energy band structure and extend the
absorption edge of CeO₂ towards a wider light region
effectively.^[46] Plots of the energy band structures for fluorite-type

CeO₂ and RE-doped CeO₂ are outlined in Figure S6. The energy band structures of YC and LC are similar with that of pure CeO₂, and similar values of the band gap are consistent with UV-vis results. Interestingly, it was found that new features appear in the band gaps of SC and NC (Figure S6 (b) and (e)), which are contributed to the overlap of energy levels between the states of dopants (Sm and Nd) and the O, resulting in the dopants–O binding. The exist of impurity energy levels significantly change the band structures and narrow the band gap, bringing higher light yield.

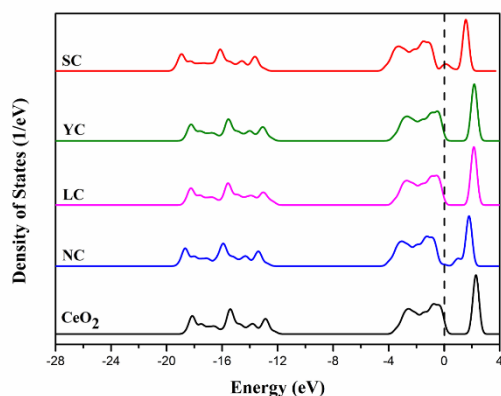


Figure 8. Density of states (DOS) of all samples.

Based on all observed characterization results and the results of photocatalytic evaluation experiments, a reasonable reaction mechanism of RE ion-doped CeO₂ is proposed (Figure 9). The introduction of RE ions into the cubic fluorite structure of CeO₂ can affect its crystal structure evidently. After an incorporation of RE ions, the surface exposed cerium ions are partly substituted by those cations, resulting in a higher concentration of oxygen vacancies (O_v), which leads to a formation of doping transition states. Then more O_v can efficiently capture electrons in the conduction band (CB) and limit the recombination rate of photo-generated electrons and holes in doped-CeO₂. These transition states caused by doping can extend lifetime of photo-generated carriers during the migration process and further lead to an effective separation efficiency of photo-generated carriers. Additionally, abundant hydroxyl radicals ($\cdot\text{OH}$) and superoxide radical ($\cdot\text{O}_2^-$) can be generated in the VB and CB, respectively. The higher concentration of $\cdot\text{OH}$ and $\cdot\text{O}_2^-$ are both highly efficient intermediates with vivid oxidation ability to further react with organic compounds, leading to an outstanding enhancement of photooxidation performance. Based on the experiments of BPA degradation and of CH₃CHO decomposition, we can draw conclusions that the photocatalytic performance is apparently enhanced after different RE ions doping and SC possesses the highest photooxidation activity among them. The reasons maybe attribute to the following two factors, one is that the ionic radius of Sm³⁺ is closer to Ce⁴⁺, leading to the entry of ions into the interior of the lattice much more easily and readily. The introduction of Sm ions leads to an expansion of the crystal lattice in CeO₂, which is more convenient for the transmission of electrons. And those migrated electrons can hasten the diffusion rate of oxygen and boost reactive oxygen species (ROS) effectively. The other reason is that Sm has two

variable valence states and those two states will provide much more oxygen vacancies, which represents that they can further restrict the recombination rate of photogenerated carriers, then lead to an efficient promotion of the photocatalytic activity. Thus, RE ions doping is a feasible strategy to enhance the photocatalytic efficiency of traditional semiconductors.

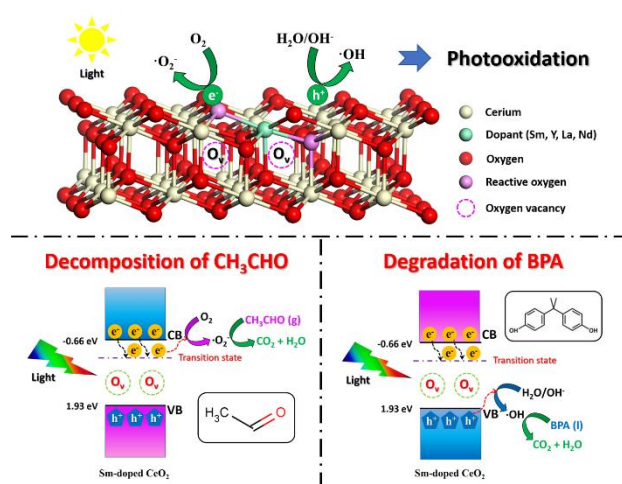


Figure 9. A proposed mechanism for photocatalytic performance enhancement.

Conclusion

In summary, CeO₂ photocatalysts doped with different RE ions were successfully prepared by a template-free hydrothermal treatment. This method for design and synthesis is cost-effective and can be easily extended to the manufacture of other RE ion-doped inorganic semiconductor materials. FE-SEM and HR-TEM images show that doped CeO₂ with a broom-like hierarchical structure is composed of numerous nanorods. Raman and XPS analyses also reveal the doped-CeO₂ has the advantage of having much more oxygen vacancies. It is found that SC exhibits superior photooxidation performance compared with that of other doped products, resulting about 3.0-times and 8.5-times higher activities than pure CeO₂ for BPA degradation and CH₃CHO decomposition, respectively. Therefore, rare earth ion-doped CeO₂ established in this paper can pave the way to fabricate other different RE ion-doped photocatalysts for energy-related and environmental remediation applications.

Experimental Section

1 Materials

Urea, cerium nitrate hexahydrate (Ce(NO₃)₃·6H₂O), sodium citrate dihydrate (C₆H₅O₇Na₃·2H₂O), yttrium nitrate hexahydrate (Y(NO₃)₃·6H₂O), lanthanum nitrate hexahydrate (La(NO₃)₃·6H₂O), samarium nitrate hexahydrate (Sm(NO₃)₃·6H₂O) and neodymium nitrate hexahydrate (Nd(NO₃)₃·6H₂O) were used in this study. All the chemical reagents used in the experiments were of analytical grade, were commercially available with 99.9% purity and were used without further purification. Deionized water was used throughout the experiments.

2 Preparation

1 First, 5.88 g $\text{CeH}_5\text{O}_7\cdot\text{Na}_3\cdot 2\text{H}_2\text{O}$ was dissolved in 140 ml deionized
 2 water and the solution was stirred vigorously at room temperature for 10
 3 min. Then 2.40 g urea was added to the solution and the solution was
 4 stirred for 30 min. The homogeneous mixture was prepared for further use.
 5 At the same time, 1.63 g $\text{Ce}(\text{NO}_3)_3\cdot 6\text{H}_2\text{O}$ and 0.144 g rare-earth salts
 6 ($\text{Sm}(\text{NO}_3)_3\cdot 6\text{H}_2\text{O}$, $\text{La}(\text{NO}_3)_3\cdot 6\text{H}_2\text{O}$, $\text{Nd}(\text{NO}_3)_3\cdot 6\text{H}_2\text{O}$ and $\text{Y}(\text{NO}_3)_3\cdot 6\text{H}_2\text{O}$)
 7 were dissolved in 20 ml deionized water with vigorous magnetic stirring at
 8 a room temperature for 30 min. Then aqueous solution of ceric and other
 9 rare-earth salts aqueous solution was dropped into the above mixture and
 10 stirred for 30 min until the solution changed to faint yellow color. The mixed
 11 solutions were then transferred into a 200 ml Teflon-lined autoclave and
 12 kept at 120 °C for 36 h. After cooling to room temperature naturally, a white
 13 precipitate was collected by centrifugation and washed with deionized
 14 water and ethanol at least three times each. Then RE-doped ceria was
 15 obtained by calcination of the as-prepared precursor in air at 500 °C for 4
 16 h to collect the final faint yellow product. For simplification, samples of Sm-
 17 doped CeO_2 , Y-doped CeO_2 , La-doped CeO_2 and Nd-doped CeO_2
 18 samples are denoted as SC, YC, LC and NC, respectively.

3 Characterization

19 X-ray diffraction (XRD) was performed on a Bruker-AXS X-ray focus
 20 using a Cu K α radiation source (40 kV/40 mA). Raman spectra was
 21 obtained by an In Via Laser Confocal Raman Spectrometer. Morphology
 22 and elemental mapping of the products were observed by FE-SEM (Hitachi,
 23 S-4800) and HR-TEM (FEI, Tecnai G² F30S-TWIN, 300 KV). UV-vis
 24 diffuse reflectance spectra (DRS) was measured by a Varian Cary 5000
 25 UV-vis spectrophotometer. The X-ray photoelectron spectroscopy (XPS)
 26 experiment was carried out on a Shimadzu KRATOS AXIS-NOVA system
 27 at room temperature under 10^{-9} Pa using Al K α radiation and C 1s peak
 28 (284.6 eV) reference. Electron paramagnetic resonance (EPR) radical
 29 signal was recorded by a Bruker EPR A200 spectrometer. Photoluminescence (PL)
 30 spectroscopy measurements were performed at an excitation wavelength of 310 nm
 31 on a fluoro-spectrophotometer (Hitachi F-4500) at room temperature.

4 Bisphenol A degradation experiments

32 Photooxidation of aqueous bisphenol A (BPA) was carried out with a
 33 300 W UV lamp (light intensity = 100 mW/cm²) and temperature was
 34 controlled at 25 °C. Before the experiment, 120 mg photocatalyst and
 35 120.0 ml BPA solution (20 mg/L) were added to the reaction flask, and
 36 then an adsorption-desorption equilibrium was achieved by stirring for 1 h
 37 in a dark place. Next, the UV lamp was turned on and 4.0 mL of the
 38 suspension reaction liquid was withdrawn from the reaction flask at regular
 39 intervals. The BPA solution was separated from the photocatalyst by
 40 filtration with double layers of a cellulose acetate membrane (pore size of
 41 0.22 μm). The concentration of BPA was measured by a UV-Vis
 42 spectrophotometer (λ_{max} = 277 nm). The degradation products were
 43 determined by a high-performance liquid chromatograph (HPLC) equipped
 44 with a JASCO UV/DEC-100-VI optical detector and a chromatographic
 45 column of an Agilent eclipse XDB-C18 column (4.6 \times 150 mm) with a
 46 column temperature of 25 °C. The eluent used was a mixed solvent of
 47 acetonitrile and water (1/1, v/v). The flow rate of the mobile phase was 1
 48 ml/min. The elution was monitored at 277 nm.

5 Active species trapping experiments

49 In order to detect active species in the photodegradation process,
 50 potassium persulphate (KPS) was used as electron (e^-) scavenger,
 51 ethylenediaminetetraacetic acid disodium (EDTA) was selected as hole
 52 (h^+) scavenger, tert-butanol (TBA) was employed as hydroxyl radical ($\cdot\text{OH}$)
 53 scavenger and 1, 4-benzoquinone (BQ) was chosen as superoxide radical
 54 ($\cdot\text{O}_2^-$) scavenger. For comparison, an experiment without a scavenger was
 55 also carried out under the same conditions. The photocatalyst with
 56 different a scavenger (1 mM) was dispersed in BPA solution (120.0 ml,
 57 20 mg/L). The following process was same as the BPA photodegradation
 58 experiment described in experimental section 4.

6 Acetaldehyde decomposition experiments

59 Photooxidation activity for decomposition of acetaldehyde (CH_3CHO)
 60 was also assessed. One hundred mg of photocatalyst powder was spread
 on the bottom of a glass dish, and the glass dish was placed in a Tedlar
 bag (AS ONE Co., Ltd.). Then 500 ppm of CH_3CHO was injected into the
 bag together with 125 cm³ of artificial air. Then the bag fabricated above
 was put in a dark place at room temperature for 2 h for a purpose of
 reaching an adsorption-desorption equilibrium. A light-emitting diode lamp
 (LED; Epitex, L365) was used as a light source and its intensity was
 controlled at 1.0 mW/cm², which emitted light with a central wavelength of
 ca. 365 nm. The concentration of generated CO_2 as a function of irradiation
 time was monitored by an online gas chromatograph (Agilent
 Technologies, 3000A Micro-GC, TCD detector) equipped with OV1 and
 PLOT-Q columns.

7 Photoelectrochemical measurement experiments

61 A typical working electrode was prepared as follows: 30 mg of the
 62 photocatalyst was dispersed in 30 mL of acetone and subjected to 1-h
 ultrasonic treatment. Then single iodine (10 mg) was added to enhance its
 ionic strength and sonicated for 30 min. Next, the product was
 electroplated onto a 6 \times 1 cm conductive glass (ITO) using an
 electrophoresis method with 15 V DC power supplied for 5 min. Finally, the
 ITO glass was dried at 60 °C for 10 h to obtain the film electrode. Na_2SO_4
 (0.1 M) aqueous solution was used as the electrolyte. The working
 electrode was irradiated by a Xe arc lamp and its intensity was controlled
 at 100 mW/cm². Photoelectrochemical measurements were performed on
 an electrochemical analyzer (CHI660D, Shanghai, Chenhua) in a standard
 three-electrode configuration with Pt as the counter electrode and Ag/AgCl
 as a reference electrode.

8 Model and computational details

63 Density functional theory (DFT) computations were performed by
 64 using the CASTEP module as implemented in Materials Studio 8.0
 (Accelrys Inc.-San Diego, USA). Both the bulk crystalline cells and the
 atom positions of the pristine and doped CeO_2 were optimized within the
 generalized gradient approximation (GGA) and the exchange-correlation
 functional of Perdew-Burke-Ernzerhof (PBE). The kinetic cut-off energy for
 the plane-wave basis set was chosen to be 470 eV, the Monkhorst-Pack
 k-point meshes were set as 2 \times 2 \times 5, and the ion-electron interactions were
 modeled by the ultrasoft pseudo-potential. The convergence criteria of the
 geometry optimization for the energy change, maximum force, maximum
 stress, and maximum displacement tolerances were set to 2.0 \times 10⁻⁵
 eV/atom, 0.03 eV/Å, 0.05 GPa, and 0.001 Å, respectively. Accurate
 description of the electronic structure of rare elements is a well-known
 issue for regular DFT approaches due to the localized nature of the 4f
 electron. Hence, a tunable Hubbard type correction term should be
 included into the DFT framework: DFT + U. The value of U for Ce, Sm, Y,
 La, Nd was 6 eV. The super-cells used are the fluorite cubic 2 \times 2 \times 1 cell
 with 48 atoms. Replacing a single Ce atom with Sm, Y, La and Nd
 elements results in dopant concentrations of 6.25%.

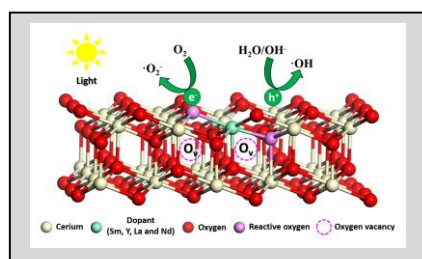
Acknowledgements

65 This work was supported by the Natural Science Foundation
 of Guangdong Province (Grant No. 2020A151501982), the Major
 Projects of Nature Science Research in Universities and Colleges
 in Jiangsu Province, China (Grant No. 16KJA150008), the Natural
 Science Foundation of China (Grant No. 21805191) and the JST
 ACT-C program of Japan

Keywords: Doped Ceria • Hierarchical structure • Oxygen
 vacancies • Photooxidation

- [1] N. Patel, R. Jaiswal, T. Warang, G. Scarduelli, *Applied Catalysis B: Environmental*, **2014**, 150, 74-81.
- [2] Y. Wang, H. Arandiyan, J. Scott, A. Bagheri, H. Dai, *Journal of Materials Chemistry A*, **2017**, 5, 8825-8846.
- [3] H. Xu, Z. Qu, C. Zong, W. Huang, F. Quan, N. Yan, *Environmental Science Technology*, **2015**, 49, 6823-6830.
- [4] H.J. Kim, G. Lee, M.G. Jang, K.J. Noh, J.W. Han, *ChemCatChem*, **2019**, 11, 2288-2296.
- [5] M.K. Gnanamani, G. Jacobs, W.D. Shafer, B.H. Davis, *ChemCatChem*, **2017**, 9, 492-498.
- [6] B. Chen, X. Li, R. Zheng, R. Chen, X. Sun, *Journal of Materials Chemistry A*, **2017**, 5, 13382-13391.
- [7] S. Yuán, S. Liu, Q. Zhang, M. Zhang, B. Xu, T. Ohno, *ChemCatChem*, **2018**, 10, 1-6.
- [8] S. Yuan, Q. Zhang, B. Xu, Z. Jin, M. Zhang, T. Ohno, *RSC Advance*, **2014**, 4, 62255-62261.
- [9] B. Xu, Q. Zhang, S. Yuan, M. Zhang, T. Ohno, *Chemical Engineering Journal*, **2015**, 260, 126-132.
- [10] B. Choudhury, P. Chetri, A. Choudhury, *RSC Advance*, **2014**, 4, 4663-4671.
- [11] Y. Huang, Y. Lu, Y. Lin, Y. Mao, G. Ouyang, H. Liu, *Journal of Materials Chemistry A*, **2018**, 6, 24740-24747.
- [12] B. Mandal, A. Mondal, S.S. Ray, A. Kundu, *Dalton Transactions*, **2016**, 45, 1679-1692.
- [13] F. Dvořák, O. Stetsovych, M. Steger, E. Cherradi, I. Matolínová, *The Journal of Physical Chemistry C*, **2011**, 115, 7496-7503.
- [14] L.-W. Qian, X. Wang, H.-G. Zheng, *Crystal Growth & Design*, **2011**, 12, 271-280.
- [15] D. Channei, B. Inceesungvorn, N. Wetchakun, Phanichphant, *Scientific Reports*, **2014**, 4, 5757.
- [16] Y. Huang, B. Long, M. Tang, Z. Rui, M.-S. Balogun, Y. Tong, H. Ji, *Applied Catalysis B: Environmental*, **2016**, 181, 779-787.
- [17] X. Zhou, J. Ling, W. Sun, Z. Shen, *Journal of Materials Chemistry A*, **2017**, 5, 9717-9722.
- [18] L. Truffault, M.-T. Ta, T. Devers, K. Konstantinov, *Materials Research Bulletin*, **2010**, 45, 527-535.
- [19] J. Saranya, K.S. Ranjith, P. Saravanan, D. Mangalaraj, R.T. Rajendra Kumar, *Materials Science in Semiconductor Processing*, **2014**, 26, 218-224.
- [20] C. Siritwong, N. Wetchakun, B. Inceesungvorn, *Progress in Crystal Growth and Characterization of Materials*, **2012**, 58, 145-163.
- [21] D. Jampaiah, K.M. Tur, S.J. Ippolito, Y.M. Sabri, *RSC Advances*, **2013**, 3, 12963.
- [22] E. Sasmaz, C. Wang, M.J. Lance, J. Lauterbach, *Journal of Materials Chemistry A*, **2017**, 5, 12998-13008.
- [23] W.L. Wang, W.Y. Liu, X.L. Weng, Y. Shang, J.J. Chen, Z.G. Chen, Z.B. Wu, *Journal of Materials Chemistry A*, **2018**, 6, 866-870.
- [24] X. Zhang, X. Xie, H. Wang, J. Zhang, B. Pan, *Journal of the American Chemical Society*, **2013**, 135, 18-21.
- [25] Y. Lee, G. He, A.J. Akey, R. Si, M. Flytzani-Stephanopoulos, I.P. Herman, *Journal of the American Chemical Society*, **2011**, 133, 12952-12955.
- [26] S. Chang, M. Li, Q. Hua, L. Zhang, Y. Ma, B. Ye, W. Huang, *Journal of Catalysis*, **2012**, 293, 195-204.
- [27] Z.D. Dohčević-Mitrović, M. Grujić-Brojčin, M. Šćepanović, *Journal of Physics: Condensed Matter*, **2006**, 18, S2061-S2068.
- [28] A. Tovt, L. Bagolini, F. Dvořák, N.-D. Tran, *Journal of Materials Chemistry A*, **2019**, 7, 13019-13028.
- [29] L. Ma, D. Wang, J. Li, B. Bai, L. Fu, Y. Li, *Applied Catalysis B: Environmental*, **2014**, 148, 36-43.
- [30] M.S. Minjoong Yoon, Cheoljin Jeong, Joon Hee Jang, and Ki Seok Jeon, *Chemistry of Materials*, **2005**, 17, 6069-6079.
- [31] R. Ma, M. Jahurul Islam, D. Amaranatha Reddy, T.K. Kim, *Ceramics International*, **2016**, 42, 18495-18502.
- [32] S. Hu, F. Zhou, L. Wang, J. Zhang, *Catalysis Communications*, **2011**, 12, 794-797.
- [33] M.J. Islam, D.A. Reddy, J. Choi, T.K. Kim, *RSC Advances*, **2016**, 6, 19341-19350.
- [34] Z.a. Huang, Q. Sun, K. Lv, Z. Zhang, M. Li, B. Li, *Applied Catalysis B: Environmental*, **2015**, 164, 420-427.
- [35] P. Dumrongrojthanath, T. Thongtem, A. Phuruangrat, *Superlattices and Microstructures*, **2013**, 54, 71-77.
- [36] F. Deng, Y. Liu, X. Luo, D. Chen, S. Wu, *Separation and Purification Technology*, **2013**, 120, 156-161.
- [37] K. Kondo, N. Murakami, T. Tsubota, T. Ohno, *Applied Catalysis B: Environmental*, **2013**, 142, 362-367.
- [38] Z. Jin, N. Murakami, T. Tsubota, T. Ohno, *Applied Catalysis B: Environmental*, **2014**, 150, 479-485.
- [39] P. Patsalas, S. Logothetidis, L. Sygellou, S. Kennou, *Physical Review B*, **2003**, 68, 035104.
- [40] D. Jampaiah, S.J. Ippolito, Y.M. Sabri, B.M. Reddy, *Catalysis Science & Technology*, **2015**, 5, 2913-2924.
- [41] S. Hu, F. Zhou, L. Wang, J. Zhang, *Catalysis Communications*, **2011**, 12, 794-797.
- [42] H. Yang, B. Xu, S. Yuan, Q. Zhang, M. Zhang, T. Ohno, *Applied Catalysis B: Environmental*, **2019**, 243, 513-521.
- [43] W. Liu, L. Cao, W. Cheng, Y. Cao, X. Liu, W. Zhang, X. Mou, L. Jin, X. Zheng, W. Che, Q. Liu, T. Yao, S. Wei, *Angew Chem Int Ed Engl*, **2017**, 56, 9312-9317.
- [44] N. Tian, H. Huang, C. Liu, F. Dong, T. Zhang, X. Du, S. Yu, Y. Zhang, *Journal of Materials Chemistry A*, **2015**, 3, 17120-17129.
- [45] P. Ji, J. Zhang, F. Chen, M. Anpo, *Applied Catalysis B: Environmental*, **2009**, 85, 148-154.
- [46] Y. Xue, D. Tian, D. Zhang, C. Zeng, *Computational Materials Science*, **2019**, 158, 197-208.

Entry for the Table of Contents



CeO₂ doped with Sm, Y, La and Nd having a broom-like hierarchical structure was successfully synthesized. The enhanced photocatalytic activity can be attributed to a higher concentration of oxygen vacancies caused by doping. During the process of photocatalytic degradation, abundant highly reactive hydroxyl radicals ($\cdot\text{OH}$) and superoxide radicals ($\cdot\text{O}_2^-$) are efficient intermediates with vivid oxidation ability.



Click here to access/download
Supporting Information
Supplementary Material.docx

